Research article

Theoretical study of the effect of halogen substitution in molecular porous materials for CO_2 and C_2H_2 sorption

Douglas M. Franz, Mak Djulbegovic, Tony Pham* and Brian Space*

Department of Chemistry, University of South Florida, 4202 East Fowler Avenue, CHE205, Tampa, FL 33620-5250, USA

* **Correspondence:** Email: tpham4@mail.usf.edu; brian.b.space@gmail.com;
  Tel: +1-813-765-4846.

Abstract: Grand canonical Monte Carlo (GCMC) simulations of carbon dioxide (CO_2) and acetylene (C_2H_2) sorption were performed in MPM-1-Cl and MPM-1-Br, two robust molecular porous materials (MPMs) that were synthesized by the addition of adenine to CuX_2 (X = Cl or Br) by solvent diffusion. Previous experimental studies revealed that both MPMs are selective for C_2H_2 over CO_2 [Xie DY, et al. (2017) *CIESC J* 68: 154–162]. Simulations in MPM-1-Cl and MPM-1-Br were carried out using polarizable and nonpolarizable potentials of the respective sorbates; this was done to investigate the role of explicit induction on the gas sorption mechanism in these materials. The calculated sorption isotherms and isosteric heat of adsorption (Q_{st}) values for both sorbates are in reasonable agreement with the corresponding experimental measurements, with simulations using the polarizable models producing the closest overall agreement. The modeled CO_2 binding site in both MPMs was discovered as sorption between the halide ions of two adjacent $[Cu_2(adenine)_4X_2]^{2+}$ (X = Cl, Br) units. In the case of C_2H_2, it was found that the sorbate molecule prefers to align along the X–Cu–Cu–X axis of the copper paddlewheels such that each H atom of the C_2H_2 molecule can interact favorably with the coordinated X^- ions. The simulations revealed that both MPMs exhibit stronger interactions with C_2H_2 than CO_2, which is consistent with experimental findings. The effect of halogen substitution toward CO_2 and C_2H_2 sorption in two isostructural MPMs was also elucidated in our theoretical studies.

Keywords: metal–organic framework; simulation; gas sorption; carbon dioxide; acetylene; gas separation

1. Introduction

Metal–organic materials (MOMs) are a class of synthesized, often porous, and crystalline materials that have comprised the focus of a large amount of experimental and theoretical studies for the past

few decades [1–3]. The application of MOMs is very diverse and has become essentially ubiquitous in scientific research, ranging from gas sorption [3–17], separation [4, 18, 19], catalysis [20–23], sensing [24, 25], photoinduced electron transfer [26–29] and biological uses [30, 31]. The major reason for this is that there are conceivably infinite variations of MOM structures that can be synthesized by altering their component metal ions, organic linkers, secondary building units (SBUs) [32, 33], solvents, and thermodynamic or physical conditions.

This study focuses on explaining the sorption properties of CO_2 and C_2H_2 in two isostructural porous materials. A method that separates these gases facilely from a mixture is highly sought for since CO_2 is one of the main contaminants in C_2H_2. The latter is an important feedstock chemical that is used for myriad products, such as pharmaceuticals, plastics, and fuels. There is also a growing need for technology that can mitigate the effects that CO_2 has on the environment. Indeed, the detrimental results of excess atmospheric CO_2 are both already observed and predicted to propogate in human health and the environment if steps are not taken to combat it [34]. A material that can effectively sorb and/or separate these two gases is therefore desirable and an understanding of the mechanism of such properties in candidate materials can pave the way for better, safer, and cheaper porous materials.

Recent studies involved examining C_2H_2/CO_2 separation in hybrid ultramicroporous materials (HUMs), a subclass of MOMs that combine ultramicropores with strong electrostatics from inorganic anions that line the pore surface [35, 36]. The materials of interest in this particular study are classified as molecular porous materials (MPMs), a class of molecular solids that are held together through weak noncovalent interactions (e.g., hydrogen bonding) as opposed to the conventional fully covalently bonded interactions found in most MOMs. The combination of adenine and Cu^{+2} salts of Cl and Br forms self-assembled $[Cu_2(adenine)_4Cl_2]Cl_2$ and $[Cu_2(adenine)_4Br_2]Br_2$, known as MPM-1-Cl and MPM-1-Br, respectively [37]. Orthographic views of the $1 \times 1 \times 2$ supercell of MPM-1-Br are shown in Figure 1.

The syntheses of MPM-1-Cl and MPM-1-Br are reported in references [38, 39], respectively. Both MPMs feature an interesting hydrogen-bonding network in which (1) four hydrogen atoms from four different adenine linkers are hydrogen-bonded to a single halide ion and (2) an adenine linker from one $[Cu_2(adenine)_4]^{4+}$ unit exhibits hydrogen-bonding contacts with an adenine linker from another unit. Unlike most MOMs that contain dinuclear copper paddlewheel clusters [3, 40], these MPMs contain halogen atoms bonded to the Cu^{2+} ions of the copper paddlewheels at the axial position to create a saturated metal center. The two MPMs have a minor kink in the X–Cu–Cu–X (X = Cl or Br) motif such that the angle is not 180°. Previous theoretical studies on MPMs [41] involved comparing the CO_2 and H_2 sorption mechanism in MPM-1-Cl and MPM-1-TIFSIX [42], with latter containing TiF_6^{2-} ions in place of the halide ions. Overall, MPMs are of interest due to their thermal and water stability as well as their ease of synthesis compared to most MOMs. When these attributes are combined with their decent gas sorption and separation properties, MPMs could be good and interesting candidates for materials research.

The purpose of this study is to elucidate (with atomistic resolution) the sorption properties of CO_2 and C_2H_2 in the isostructural MPM-1-Cl and MPM-1-Br analogues. Insights into the reason for why both MPMs prefer C_2H_2 over CO_2 will be obtained. Another interest of this work is examining how the electronic environment (and thus MPM–sorbate interaction) is effected by the use of a different halogen in the material. It will be shown that the van der Waals radius of the halogen and its polarizability play a key role in determining the location of the favorable sorption site and the energetics of binding in

the material. To our knowledge, this is the first study reporting simulations of C_2H_2 sorption in these materials as well as being the first theoretical study of MPM-1-Br.

(a)   (b)

(c)
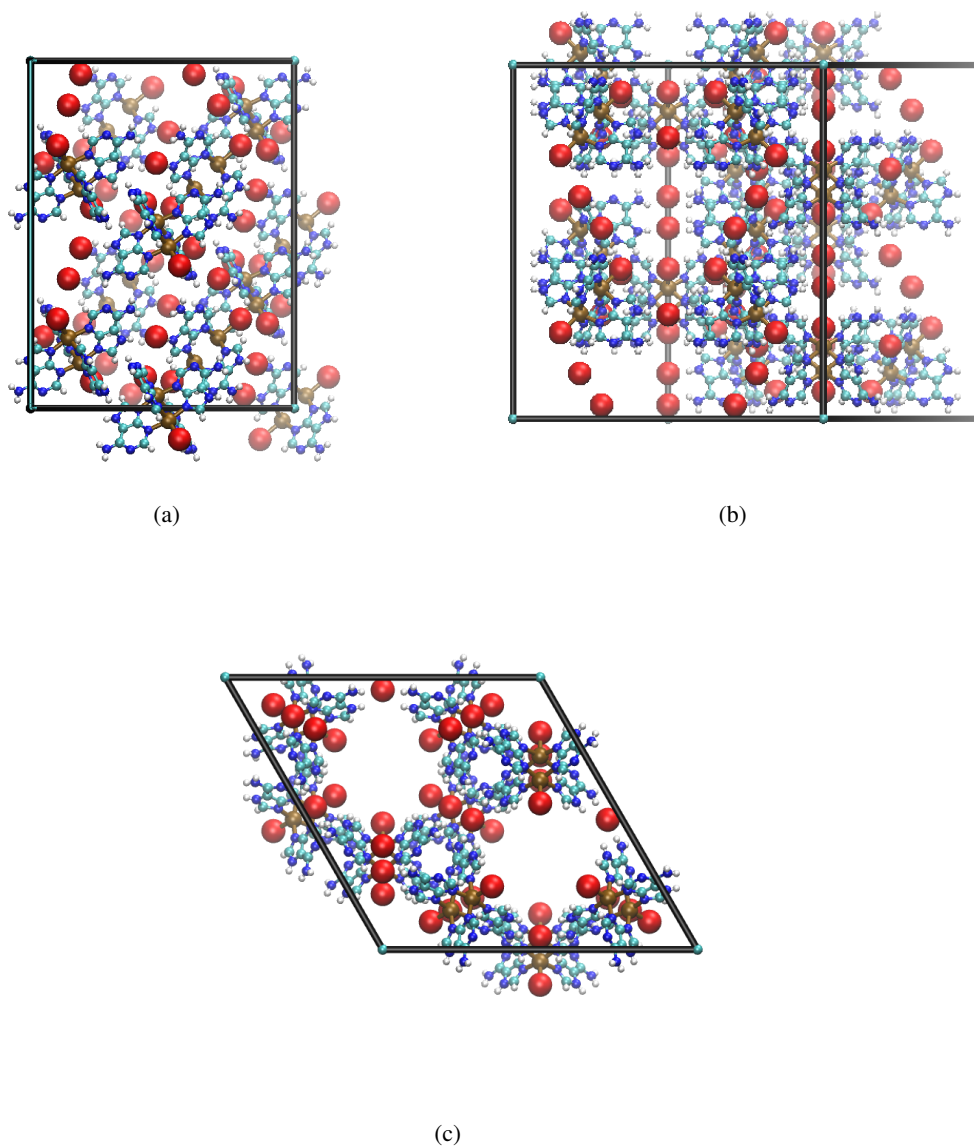
Figure 1. (a) Orthographic *a*-axis view, (b) *b*-axis view, and (c) *c*-axis view of the $1 \times 1 \times 2$ supercell of MPM-1-Br used for the simulations in this study. The crystal structure of MPM-1-Cl is very similar. Atom colors are C = cyan; N = blue; H = white; Cu = brown; Br = red.

2. Methods

The potential energy function for MPM-1-Cl was developed by our group in previous work [41] and utilized herein. The crystal structure for MPM-1-Br was obtained from reference [39]. For all

simulations in both MPMs, the sorbent atoms were treated as rigid to accomodate a constant volume ensemble system. This approximation is especially valid when phononic effects are minor [43]. As with previous work on MPM-1-Cl [41], all atoms of MPM-1-Br were given Lennard-Jones 12–6 parameters, point partial charges, and scalar point polarizabilities to model repulsion/dispersion, stationary electrostatic, and explicit polarization, respectively. The Lennard-Jones parameters for all MPM atoms were taken from the Universal Force Field (UFF) [44], while the exponentially-damped polarizabilities for all atoms other than Cu were obtained from van Duijnen et al. [45]. The polarizability parameter for Cu^{2+} was determined in reference [46] and used herein. The point partial charges for the chemically unique atoms were determined by averaging atomic charges computed via a least squares fit [47] to the electrostatic potential surface of representative MPM fragments (see Supporting Information, Figure S1) generated by quantum mechanical calculations using NWChem [48].

The potentials used for CO_2 were the nonpolarizable CO_2-PHAST [49] and TraPPE [50] models and the polarizable CO_2-PHAST* model [49]. C_2H_2-PHAST and C_2H_2-PHAST* [35,36] were used to simulate C_2H_2 sorption in both MPMs; the * denotes the inclusion of explicit polarization. Simulations of CO_2 and C_2H_2 sorption in MPM-1-Cl and MPM-1-Br were performed using grand canonical Monte Carlo (GCMC) methods [51]. The sorption simulations, theoretical isosteric heat of adsorption (Q_{st}) calculation, binding site analysis, etc. were carried out using the codes developed by our group [52,53]. Further details of performing the simulations and parametrizations are presented in the Supporting Information. All relevant simulation parameters for both MPMs and the gases simulated are also provided in the Supporting Information (Tables S1–S4).

Simulated annealing calculations were performed using the polarizable CO_2 and C_2H_2 potentials in both MPMs to determine the classical binding energy for each sorbate in the respective materials. This is a computational method which involves executing a normal Monte Carlo procedure (using the MPM with a single sorbate molecule) that is tempered by reducing the temperature with each accepted perturbation [54]. As the temperature decreases, the guest molecule settles into an energy minima whose magnitude can be compared with the Q_{st} near zero loading.

3. Summary of experimental data

3.1. C_2H_2 uptake

C_2H_2 uptake in MPM-1-Cl and MPM-1-Br was experimentally measured by Xie et al. [37] at 273 and 298 K and pressures up to 1 atm; the resulting isotherms (as estimated from [37]) are shown in Figure 2a. It can be observed that as the pressure increases at 273 K, the Cl variant exhibits mildly greater affinity for C_2H_2 than the Br analogue. This could be due to the Cl^- ions having a smaller ionic radius than Br^-, resulting in a slightly larger pore volume in MPM-1-Cl. This increased accessible volume in MPM-1-Cl relative to MPM-1-Br can allow for greater number of C_2H_2 molecules to occupy the pore space in the material at conditions approaching saturation.

Interestingly, the relative uptake trend is reversed at 298 K: MPM-1-Br shows slightly greater affinity for C_2H_2 compared to MPM-1-Cl for all pressures considered at this temperature. The observed phenomenon may be caused by the increased kinetic energy of the C_2H_2 molecules and the Br variant at higher temperatures. This permits the C_2H_2 molecules to diffuse through and collide with MPM-1-Br at a greater rate than at 273 K. Since Br is heavier than Cl, the Br^- ions likely vibrate

more slowly than the Cl$^-$ ions, thus making MPM-1-Br more rigid. When the C$_2$H$_2$ molecules are moving more quickly at higher temperatures, the favorable geometry of the MPM-1-Br framework is less flexible, whereas the higher kinetic energy of gas molecules may induce a slightly unfavorable conformational change for the Cl analogue. This is further emphasized from the fact that the primary binding site discovered for C$_2$H$_2$ in MPM-1-Br has a lower potential energy and closer distance to the Cu paddlewheel than the analogous site in MPM-1-Cl; this will be explained below in Section 4.3.
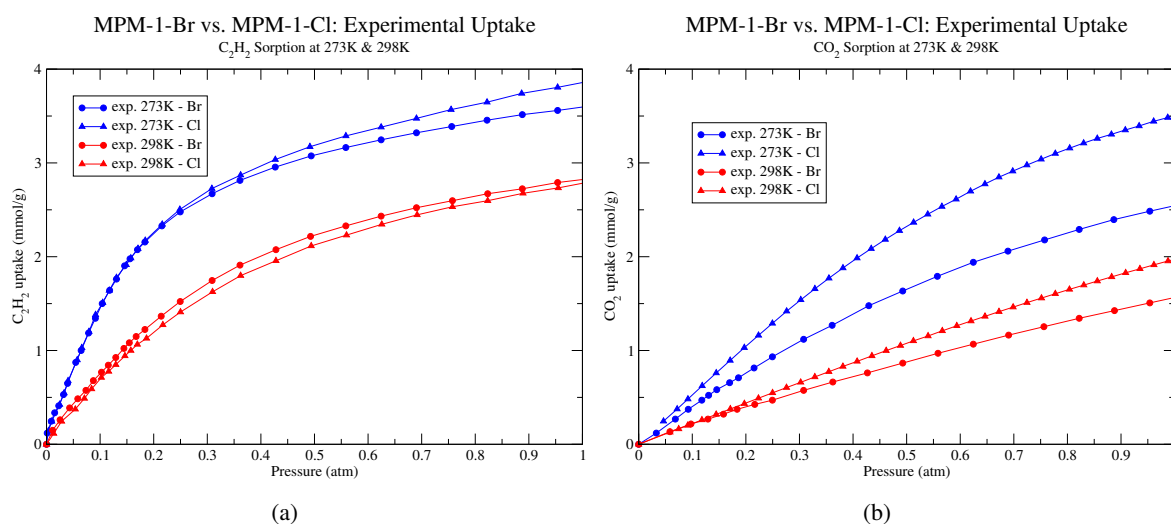
Figure 2. Experimental gas sorption isotherms of (a) C$_2$H$_2$ and (b) CO$_2$ for MPM-1-X (X = Br, circles or Cl, triangles). at two different temperatures (blue = 273 K; red = 298 K) and pressures up to 1 atm. All experimental data were estimated from [37].

3.2. CO$_2$ uptake

Xie et al. also measured CO$_2$ sorption in MPM-1-Cl and MPM-1-Br under the same conditions as C$_2$H$_2$ [37]; these isotherms are presented in Figure 2b. We note that Zaworotko's group also reported CO$_2$ sorption data in the Cl analogue previously [41, 42]. It can be seen that MPM-1-Cl sorbs a greater quantity of CO$_2$ for nearly all state points considered. This phenomenon may be explained by Cl exhibiting a higher electronegativity than Br, which allows for greater electrostatic interactions between the halide ion and the CO$_2$ molecule. Although CO$_2$ has no permanent dipole moment in the bulk, it displays high induced dipoles when interacting with the MPM framework [41]. The interaction between the Cl$^-$ ion and the partial positive carbon atom of the CO$_2$ molecule is fortified with a greater electronegativity compared to Br$^-$. Our electronic structure calculations in both MPMs confirmed that the magnitude of the partial negative charges of the Cl$^-$ ions in MPM-1-Cl are greater than those for the Br$^-$ ions in MPM-1-Br (see Supporting Information, Table S1).

3.3. Isosteric heats of adsorption

Xie et al. [37] derived the experimental Q_{st} values for C$_2$H$_2$ and CO$_2$ in MPM-1-Cl and MPM-1-Br by applying the virial method [55] to the corresponding experimental isotherms. These Q_{st} values are plotted as a function of gas loading in Figure 3. For both MPMs, the Q_{st} for C$_2$H$_2$ is higher than that

for CO_2 at all loadings considered, thus indicating that these two MPMs display greater preference for C_2H_2 over CO_2. Table 1 provides a summary of the zero-loading Q_{st} values (Q_{st}^0) for C_2H_2 and CO_2 in both MPMs.
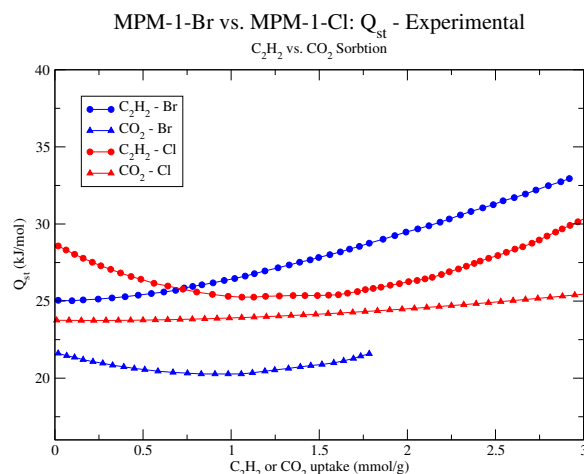
Figure 3. Experimental isosteric heats of adsorption (Q_{st}) for C_2H_2 (circles) and CO_2 (triangles) for MPM-1-X (X = Br, blue or Cl, red). All experimental data were estimated from [37].

Table 1. Summary of data from key state points for gas sorption in MPM-1-Cl and MPM-1-Br. Experimental values [37] are compared with simulation using various potentials for each sorbate. Q_{st}^0 is the Q_{st} value for the lowest reported loading. Units are [a]kJ mol^{-1}, [b]mmol g^{-1}.

	CO$_2$				C$_2$H$_2$		
MPM-1-Cl	Exp.	Simulation			Exp.	Simulation	
Model		CO$_2$-PHAST*	CO$_2$-PHAST	TraPPE		C$_2$H$_2$-PHAST*	C$_2$H$_2$-PHAST
$Q_{st}^{0\,a}$	23.76	22.77	24.33	26.22	28.57	25.49	25.65
0.05 atm loading, 273 K^b	0.26	0.23	0.36	0.80	0.80	1.08	0.81
1.0 atm loading, 273 K^b	3.50	3.63	4.75	5.06	3.86	5.05	5.25
0.05 atm loading, 298 K^b	0.12	0.13	0.17	0.35	0.34	0.34	0.25
1.0 atm loading, 298 K^b	1.97	2.07	2.74	3.60	2.78	4.21	4.57
MPM-1-Br	Exp.	Simulation			Exp.	Simulation	
Model		CO$_2$-PHAST*	CO$_2$-PHAST	TraPPE		C$_2$H$_2$-PHAST*	C$_2$H$_2$-PHAST
$Q_{st}^{0\,a}$	21.61	25.02	25.57	25.40	25.05	30.61	27.55
0.05 atm loading, 273 K^b	0.19	0.23	0.33	0.51	0.81	1.41	1.23
1.0 atm loading, 273 K^b	2.54	2.52	3.20	3.77	3.59	3.69	3.66
0.05 atm loading, 298 K^b	0.12	0.11	0.13	0.20	0.43	0.34	0.22
1.0 atm loading, 298 K^b	1.56	1.52	1.80	2.47	2.82	3.31	3.30

With regards to C_2H_2, MPM-1-Cl exhibits a Q_{st}^0 value of 28.57 kJ mol^{-1}, while that for MPM-1-Br is 25.05 kJ mol^{-1}. This suggests that MPM-1-Cl displays a more favorable initial loading site for C_2H_2 than MPM-1-Br according to experiment. The C_2H_2 Q_{st} plot for MPM-1-Cl exhibits an expected decrease in Q_{st} with each successive C_2H_2 molecule sorbed in the MPM at low loading; however, after ~1.5 mmol g^{-1} loading is reached, the Q_{st} values begin to increase and eventually surpass the Q_{st}^0 value. The analogous plot for MPM-1-Br shows that the Q_{st} continually increases as the loading increases. Overall, for both MPMs, the increase in Q_{st} as a function of loading could be due

to a combination of MPM–sorbate and cooperative sorbate–sorbate interactions [41, 56]. Interestingly, while the experimentally reported C_2H_2 Q_{st} for MPM-1-Br is higher than that for MPM-1-Cl at high loadings (>1 mmol g^{-1}), the reported C_2H_2 uptake is higher for MPM-1-Cl at 273 K and high pressures. We believe that this could be due to the empirical fitting method employed to obtain the Q_{st} values from experimental isotherms. This is discussed in more detail in Section 4.1.3.

The Q^0_{st} value for CO_2 in MPM-1-Cl and MPM-1-Br is 23.76 and 21.61 kJ mol^{-1}, respectively. Further, the CO_2 Q_{st} for MPM-1-Cl is greater than that for MPM-1-Br across the considered loading range. This implies that CO_2 sorption is more favorable in MPM-1-Cl than MPM-1-Br, presumably due to the greater electronegativity and calculated partial negative charge of the Cl$^-$ ion as explained in the previous subsection. Interestingly, the CO_2 Q_{st} plot for MPM-1-Cl shows the same behavior as the C_2H_2 Q_{st} plot for MPM-1-Br. Likewise, the shape of the Q_{st} plot for CO_2 in MPM-1-Br is similar to that for the C_2H_2 Q_{st} plot for MPM-1-Cl. As with C_2H_2, both MPMs exhibit increasing Q_{st} with increasing loading in their CO_2 Q_{st} plots, which indicates that CO_2–CO_2 interactions are favorable in these materials.

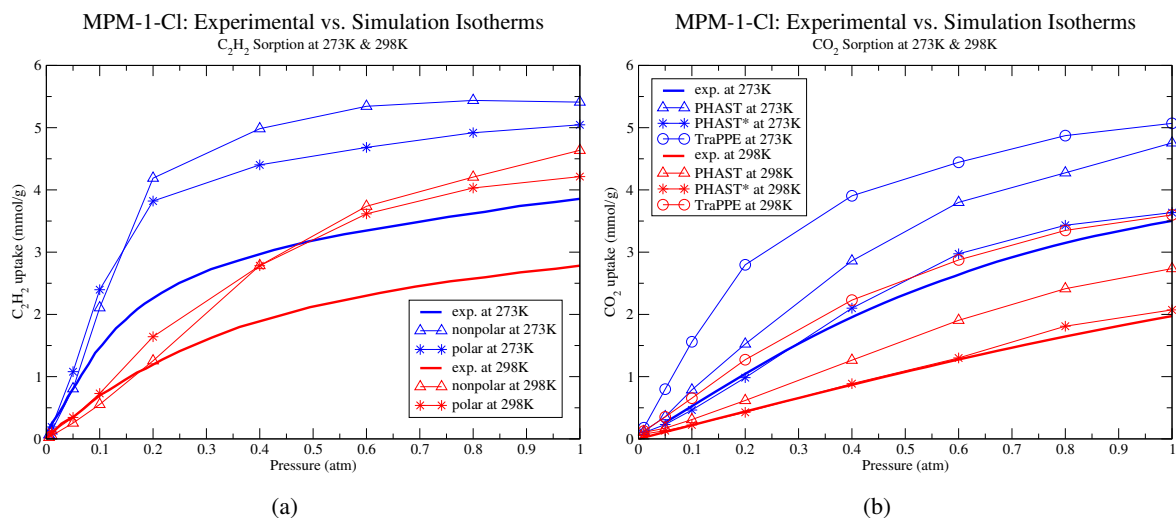## 4. Simulation results and discussion
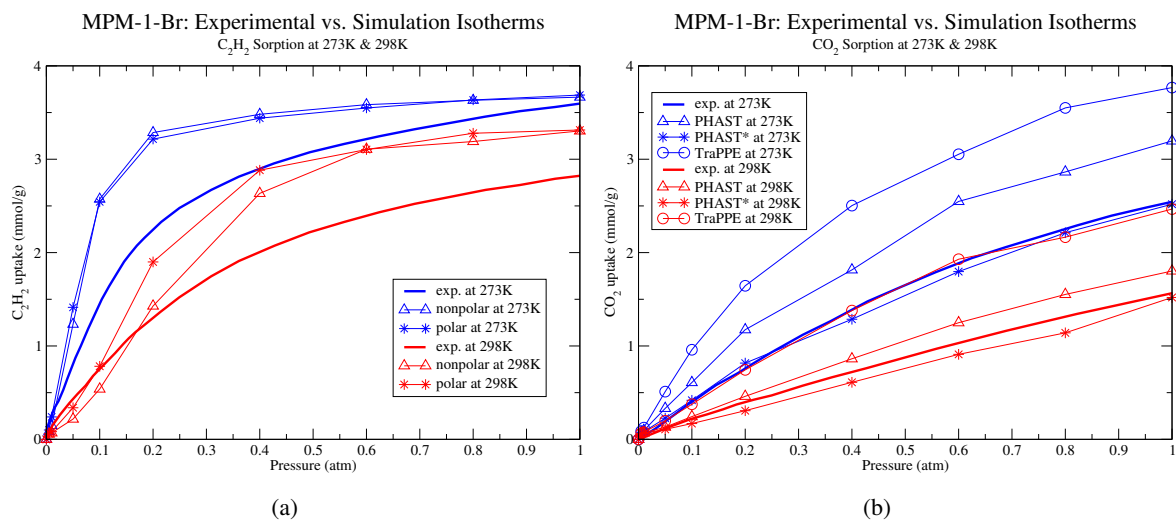
4.1. C_2H_2 sorption

4.1.1. MPM-1-Cl

The experimental and simulated C_2H_2 sorption isotherms in MPM-1-Cl at 273 and 298 K are displayed in Figure 4a. At 273 K, the calculated uptakes for the nonpolarizable C_2H_2-PHAST and polarizable C_2H_2-PHAST* models are in good agreement with experiment at pressures of 0.05 atm and lower. At higher pressures, however, the simulated uptakes for both potentials are significantly higher than experiment. At 298 K, both models generated sorption isotherms that show very good agreement with experiment for pressures up to 0.2 atm, while they notably oversorb experiment at greater pressures. The fact that the simulated uptakes for the two potentials are in close agreement with experiment at low pressures for both temperatures suggest proper modeling of the initial C_2H_2 binding sites in this material. The significant oversorption compared to experiment implies that the simulations produced inflated sorbate–sorbate interactions in the MPM relative to what is physically captured in experiment, which could be attributed to inadequacies in the present C_2H_2 potentials. It can be observed that the polarizable model produced uptakes that are somewhat closer to experiment at higher pressures.

4.1.2. MPM-1-Br

Figure 5a shows the simulated C_2H_2 sorption isotherms in MPM-1-Br at 273 and 298 K compared to experiment. As with MPM-1-Cl, simulations using the C_2H_2-PHAST and C_2H_2-PHAST* models in MPM-1-Br at both temperatures generally produced uptakes that are in good agreement with experiment at low pressures and those that are remarkably higher than experiment at higher pressures. Both models yielded comparable isotherms in MPM-1-Br at 273 K, with uptakes that are in closer agreement with experiment as the pressure approaches 1 atm. This could be a consequence of the material reaching C_2H_2 saturation under these conditions. At 298 K, the uptakes for the C_2H_2-PHAST* model is in better agreement with experiment at pressures lower than 0.1 atm.

MPM-1-Cl: Experimental vs. Simulation Isotherms
C₂H₂ Sorption at 273K & 298K

MPM-1-Cl: Experimental vs. Simulation Isotherms
CO₂ Sorption at 273K & 298K

Figure 4. Simulated gas sorption isotherms of (a) C_2H_2 and (b) CO_2 for MPM-1-Cl compared with experiment at two different temperatures (blue = 273 K; red = 298 K) and pressures up to 1 atm. Experiment = pure solid line; C_2H_2/CO_2-PHAST model = solid line with triangles; C_2H_2/CO_2-PHAST* model = solid line with stars; TraPPE model = solid line with circles.

MPM-1-Br: Experimental vs. Simulation Isotherms
C₂H₂ Sorption at 273K & 298K

MPM-1-Br: Experimental vs. Simulation Isotherms
CO₂ Sorption at 273K & 298K

Figure 5. Simulated gas sorption isotherms of (a) C_2H_2 and (b) CO_2 for MPM-1-Br compared with experiment at two different temperatures (blue = 273 K; red = 298 K) and pressures up to 1 atm. Experiment = pure solid line; C_2H_2/CO_2-PHAST model = solid line with triangles; C_2H_2/CO_2-PHAST* model = solid line with stars; TraPPE model = solid line with circles.

As shown in Table 1, the experimental C_2H_2 uptakes for MPM-1-Br at both temperatures are higher than those for MPM-1-Cl at low pressures (0.05 atm), whereas such uptakes for the former are lower than those for the latter at higher pressures (1.0 atm). This trend is consistent with what was observed in the simulations when utilizing both C_2H_2 potentials. Therefore, MPM-1-Br exhibits greater interactions with the C_2H_2 molecules than MPM-1-Cl at low loadings, which could be explained by the Br^- ions having a larger polarizability and van der Waals parameters than Cl^- ions (see Supporting Information, Table S2). Nevertheless, at higher pressures, MPM-1-Br displays lower C_2H_2 uptake than the Cl analogue because less accessible space is available in the material under these conditions due to the larger ionic radius of the Br^- ions. Indeed, the shape of the simulated C_2H_2 sorption isotherms for MPM-1-Br suggests that the material is near C_2H_2 saturation at *ca.* 3.5 mmol g^{-1} loading.

4.1.3. Isosteric heats of adsorption

The simulated C_2H_2 Q_{st} values for MPM-1-Cl and MPM-1-Br are compared with their corresponding experimental Q_{st} plots in Figures 6a and 7a, respectively. It can be observed that simulations using the two models captured the apparent increase in Q_{st} as the loading increases for both MPMs. This shape is consistent with the experimental C_2H_2 Q_{st} plot for MPM-1-Br. Overall, the trend in the simulated Q_{st} values for MPM-1-Cl and MPM-1-Br support the experimental observation that both MPMs tend to facilitate C_2H_2 sorption such that initially loaded molecules tend to cooperatively interact with each other to lower the potential energy of subsequent guest molecules, thereby leading to enhanced sorbate–sorbate interactions at higher loadings. When considering all loadings, both models produced Q_{st} values that are within the vicinity of experiment for both MPMs.

The theoretical Q_{st}^0 value for the C_2H_2-PHAST and C_2H_2-PHAST* models in MPM-1-Cl are 25.49 and 25.65 kJ mol^{-1}, respectively, which are lower than the corresponding experimental value of 28.57 kJ mol^{-1} (Table 1). Simulations in MPM-1-Br yielded Q_{st}^0 values of 30.61 and 27.55 kJ mol^{-1} for the nonpolarizable and polarizable models, respectively, which are higher than the experimental value for this MPM (25.05 kJ mol^{-1}). In general, our simulations suggest that MPM-1-Br exhibits a higher Q_{st}^0 value for C_2H_2 than MPM-1-Cl, whereas the opposite trend is observed according to experiment. From a molecular point of view, it is expected that MPM-1-Br would display a greater affinity for C_2H_2 due to the higher polarizability of the Br^- ions. Such an effect is probably captured in our simulations that include both implicit and explicit polarization. This behavior is not reflected in the reported experimental C_2H_2 Q_{st} for both MPMs even though the experimental isotherms at both temperatures suggest that MPM-1-Br outperforms MPM-1-Cl for C_2H_2 uptake at low pressures (see Table 1). It is notable that the experimental Q_{st} values are derived from an empirical fitting procedure on the measured sorption isotherms, whereas the theoretical values are obtained directly from GCMC simulation [57]. We could therefore attribute the discrepancy in the relative Q_{st}^0 trend between experiment and simulation to the empirical fitting that was implemented to extract the experimental Q_{st} values.

4.2. CO$_2$ sorption

4.2.1. MPM-1-Cl

The simulated CO$_2$ uptakes for three different potentials (CO$_2$-PHAST, CO$_2$-PHAST*, and TraPPE) in MPM-1-Cl at 273 and 298 K are shown in Figure 4b. The isotherms produced by the CO$_2$-PHAST and TraPPE models oversorb experiment for nearly all state points considered. On the other hand, the isotherms for the CO$_2$-PHAST* model are in excellent agreement with experiment across the considered pressure range at both temperatures. The strong agreement between the experimental and simulated isotherms for the CO$_2$-PHAST* model demonstrates that this potential is highly accurate for simulations in heterogeneous media [49]. The TraPPE model yielded the highest calculated CO$_2$ uptakes in MPM-1-Cl out of all models. Indeed, at 273 K, the calculated uptakes for this model are >1.5 mmol g^{-1} higher than experiment at pressures of 0.2 atm and beyond. Although the TraPPE model is widely used, it has been shown to generate isotherms that notably oversorb experiment in many porous materials [3, 16, 58–60].

The CO$_2$-PHAST* model yielded the lowest CO$_2$ uptakes in MPM-1-Cl out of all models for all considered state points even though it includes explicit many-body polarization. Generally, the theoretical gas uptake in MOMs increases with increasing terms in the potential energy function [46]. This was not the case here as the CO$_2$-PHAST model gives uptakes that are higher than those for its polarizable counterpart. It is predicted that the inclusion of polarization produces a favorable sorbate ordering effect in this MPM, which causes the CO$_2$ uptake to decrease compared to when only stationary electrostatic interactions are considered. A similar phenomenon was observed from theoretical studies in a HUM [56]. We note that CO$_2$ sorption in MPM-1-Cl was investigated previously through GCMC simulations using only the CO$_2$-PHAST* model [41]. Herein, we show the results that were obtained using different CO$_2$ potentials in this material.

4.2.2. MPM-1-Br

A comparison of the experimental and simulated CO$_2$ sorption isotherms for the three different potentials in MPM-1-Br at 273 and 298 K is presented in Figure 5b. The results for the three models in this MPM are consistent with that for MPM-1-Cl. Notably, the isotherms for the TraPPE model significantly oversorb experiment at both temperatures. The amount of oversorption for this model is generally proportional to the pressure. The CO$_2$-PHAST model produces the next highest calculated CO$_2$ uptakes for all pressures, followed by the CO$_2$-PHAST* model. As observed in MPM-1-Cl, the CO$_2$-PHAST* model yields uptakes that are in very good agreement with experiment for all pressures at both temperatures, thus further illustrating the accuracy of this potential for simulation CO$_2$ sorption in porous materials. The isotherm for the nonpolarizable CO$_2$-PHAST model is in good agreement with experiment at 298 K, but somewhat oversorbs experiment at 273 K. The increase in temperature may provide enough kinetic energy to decrease electrostatic interactions between the Br$^-$ ions and the CO$_2$ molecule; this could explain why the CO$_2$-PHAST model shows better agreement with experiment at the higher temperature.

As shown in Table 1, the experimental atmospheric CO$_2$ uptakes in MPM-1-Br at 273 and 298 K are 2.54 and 1.56 mmol g^{-1}, respectively. The corresponding values for MPM-1-Cl are 3.50 and 1.97 mmol g^{-1}, respectively, which are higher than those for MPM-1-Br. Our simulations confirmed the experimental finding that the CO$_2$ uptakes under these thermodynamic conditions are greater for

MPM-1-Cl than MPM-1-Br; this is true regardless of the CO_2 potential that was used. It is expected that CO_2 sorption in these MPMs is governed by electrostatic interactions between the halide ion and the positively charged carbon atom of the CO_2 molecule. MPM-1-Br displays weaker interactions with the CO_2 molecules than MPM-1-Cl, probably due to the lower calculated partial negative charges for the Br^- ions compared to the Cl^- ions (see Supporting Information, Table S1). Lower magnitudes for the partial negative charge of the halide ion will result in decreased electrostatic interactions with the CO_2 molecule.

Note, we also performed simulations of CO_2 sorption in both MPMs using the EPM2 [61] model and the resulting simulated CO_2 sorption isotherms are provided in the Supplementary Information, Figure S3. The calculated isotherms for this model are comparable to those for the CO_2-PHAST model; both potentials generated uptakes that oversorb experiment at higher pressures. Overall, the polarizable CO_2-PHAST* model produced isotherms that are in closest agreement with experiment. As a result, the binding sites that are discussed later (in Section 4.3) are based on simulations using this model.

4.2.3. Isosteric heats of adsorption

The simulated CO_2 values for the CO_2-PHAST, CO_2-PHAST*, and TraPPE models for MPM-1-Cl and MPM-1-Br are displayed in Figures 6b and 7b, respectively. According to our simulations, the relative trend in the magnitude of the CO_2 Q_{st} values in both MPMs is: TraPPE > CO_2-PHAST > CO_2-PHAST*. This is consistent with the pattern that was observed for the simulated uptakes for the three models in both MPMs. The simulated Q_{st} values for the CO_2-PHAST and CO_2-PHAST* models in MPM-1-Cl are in good agreement with experiment as well as each other for all considered loadings. The TraPPE model Q_{st} values for this MPM are somewhat higher than experiment across the loading range. The Q_{st} plots for all models in MPM-1-Cl show increasing Q_{st} with higher loadings, which is consistent with the shape for the experimental plot. Therefore, our simulations captured the expected cooperative CO_2–CO_2 interactions in this MPM.

In MPM-1-Br, the Q_{st} values for all models are consistently higher than experiment for all loadings, with values produced by the polarizable CO_2-PHAST* model being closer to experiment. The experimental Q_{st} values in this MPM begins to increase when the material is partially saturated at ~1.0 mmol g^{-1} loading, indicating cooperativity between the CO_2 molecules under these conditions. Unlike in MPM-1-Cl, the Q_{st} plot for all three models in MPM-1-Br does not show much signs of sorbate–sorbate cooperativity in the material. Rather, the theoretical Q_{st} values slightly decreases with increasing CO_2 uptake, as does the experiment. In addition, the simulated Q_{st} plots level off at a loading of ~0.4 mmol g^{-1}, but there is neither a sustained or defined increasing trend in Q_{st} as the uptakes continue to increase.

The calculated Q_{st}^0 values for all three potentials in both MPMs are summarized in Table 1. The Q_{st}^0 values produced by the CO_2-PHAST, CO_2-PHAST*, and TraPPE models in MPM-1-Cl are 24.33, 22.77 and 26.22 kJ mol^{-1}, respectively, whereas the analogous quantities for the three potentials in MPM-1-Br are 25.57, 25.02 and 25.40 kJ mol^{-1}, respectively. Simulations using the CO_2-PHAST and CO_2-PHAST* potentials suggest that the MPM–CO_2 interaction is greater for MPM-1-Br than MPM-1-Cl. This is in contrast to what was observed for experiment as the empirical Q_{st}^0 value for CO_2 is higher for MPM-1-Cl than MPM-1-Br. A potential reason for why our simulations generated a higher initial loading CO_2 Q_{st} value for MPM-1-Br is explained in next section where the binding sites are

discussed.
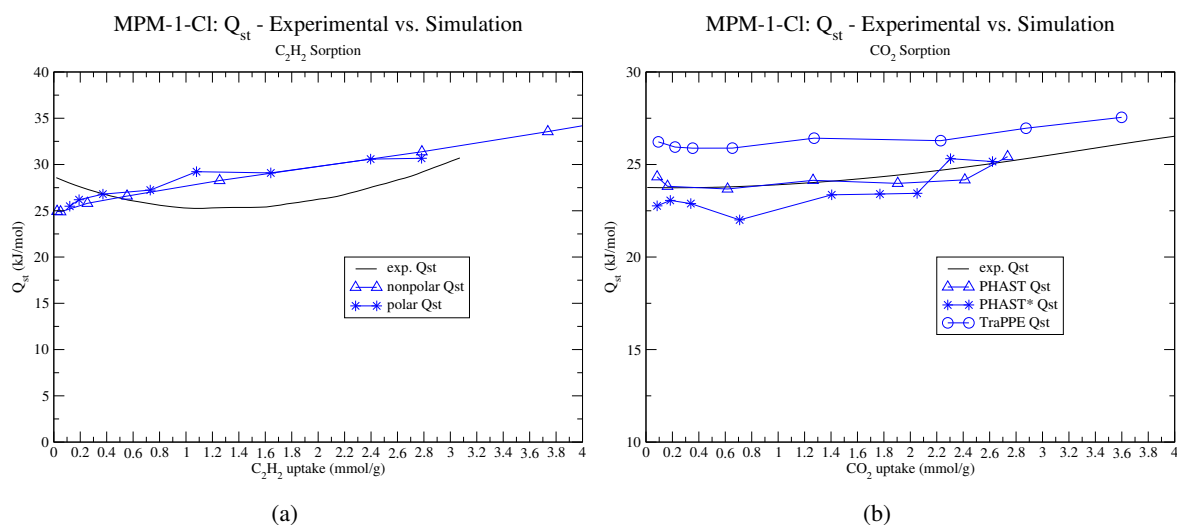
Figure 6. Simulated isosteric heat of sorption (Q_{st}) for (a) C_2H_2 and (b) CO_2 for MPM-1-Cl compared with experiment. Experiment = solid black line; Simulation = solid blue line with symbols (C_2H_2/CO_2-PHAST = triangles; C_2H_2/CO_2-PHAST* = stars; TraPPE model = circles).
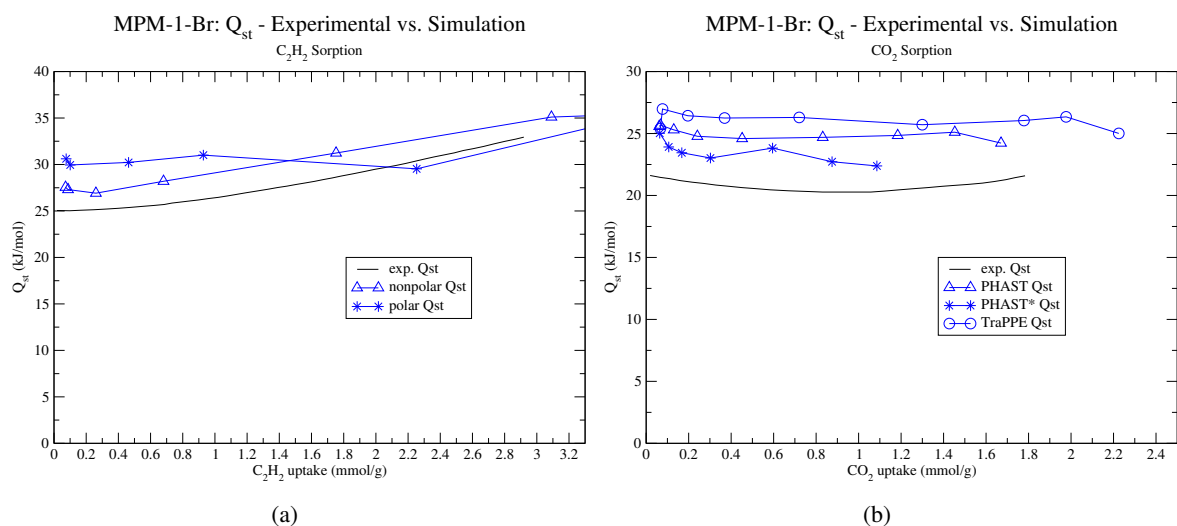
Figure 7. Simulated isosteric heat of sorption (Q_{st}) for (a) C_2H_2 and (b) CO_2 for MPM-1-Br compared with experiment. Experiment = solid black line; Simulation = solid blue line with symbols (C_2H_2/CO_2-PHAST = triangles; C_2H_2/CO_2-PHAST* = stars; TraPPE model = circles).

4.3. Binding sites

Pham et al. [41] reported a binding site for CO_2 in MPM-1-Cl in which the sorbate molecule aligns between two chlorine atoms, one that is bound to the copper paddlewheel complex and another which forms hydrogen-bonding interactions with four hydrogen atoms of two different adenine linkers (see Supporting Information, Figure S2). Interestingly, this site was minimally observed for simulations in MPM-1-Br. Indeed, the main binding site for CO_2 in MPM-1-Br was actually between two Br atoms that are coordinated to the Cu^{2+} ions of two different $[Cu_2(adenine)_4Br_2]^{2+}$ complexes (Figure 8b). Notably, the positively charged carbon atom of the CO_2 molecule can interact with two electronegative Br^- ions simultaneously. We also observed this site in MPM-1-Cl for the simulations reported herein (Figure 8a). The larger van der Waals radius of the Br^- ions causes this region to be more favorable for the CO_2 molecules in MPM-1-Br than in MPM-1-Cl. This is because the larger size of the bromide ions will result in greater close-fitting interactions with the sorbate molecules. The CO_2 molecule will exhibit a lower potential energy in the attractive well-depth potential region of both Br atoms as a result of the larger ionic radius. This could explain why the CO_2-PHAST and CO_2-PHAST* models produced CO_2 Q_{st}^0 values that are greater for MPM-1-Br.

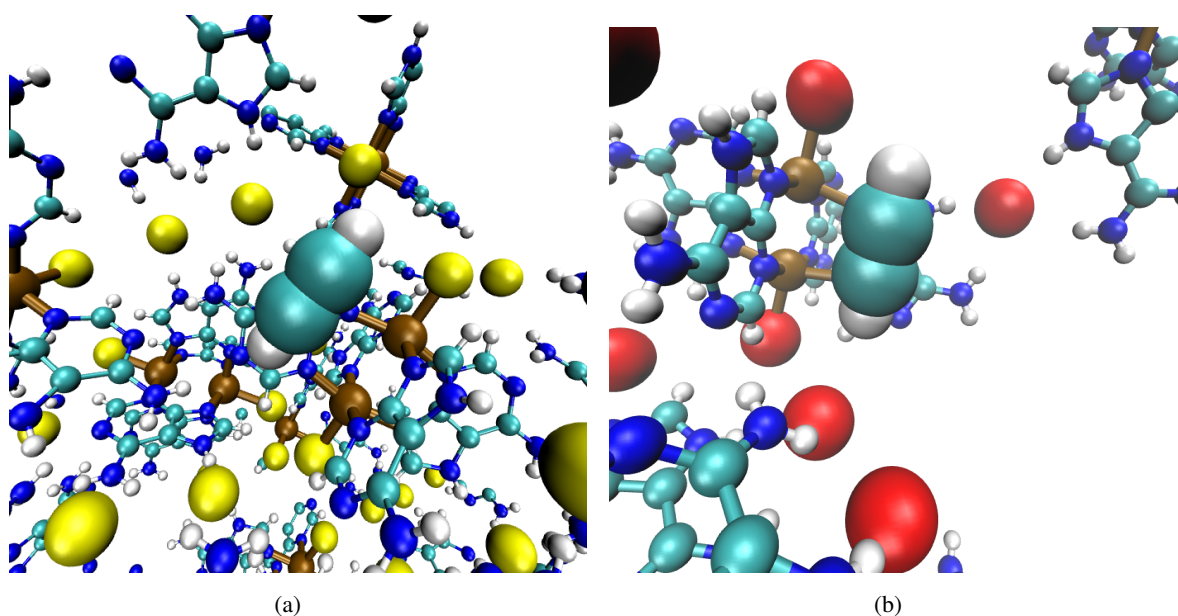(a)   (b)
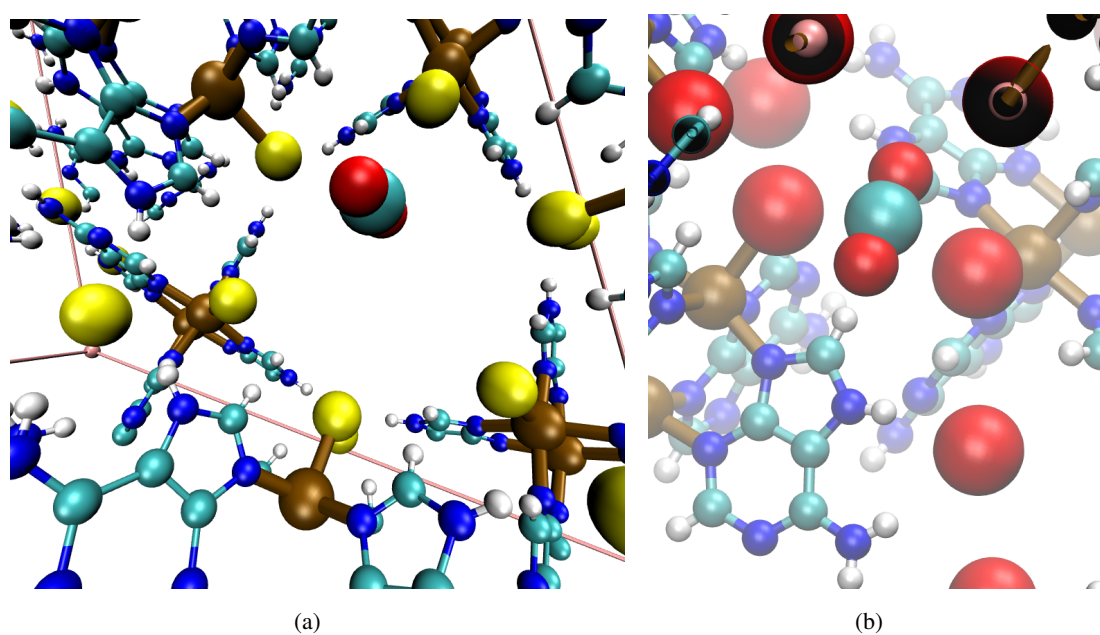
Figure 8. Molecular illustration of the primary binding site for CO_2 observed in (a) MPM-1-Cl and (b) MPM-1-Br through simulation, which is nestled between two X (X = Cl, Br) atoms bound to two different $[Cu_2(adenine)_4]^{4+}$ complexes. Atom colors are C = cyan; N = blue; H = white; Cu = brown; Cl = yellow; Br = red.

The electrostatic and electrodynamic (polarizable) effects serve to attract the positively charged carbon center of the CO_2 molecule. The Lennard-Jones mixed σ parameter for Br–C used herein is ~3.6 Å, and the measured Br–C_{CO_2} distance at the primary binding site is ~3.2 Å. The expected repulsion of the CO_2 carbon atom is therefore counteracted by the attraction of the oxygen atoms on the molecule, which (being further away from the Br atoms) reside in the well-depth region of the

dispersive potential. In addition, the calculated partial charge for this particular Br atom is $-0.51\ e^-$, which is slightly lower in magnitude than that for the analogous Cl atom in MPM-1-Cl ($-0.57\ e^-$) (see Supporting Information, Table S1). While the lower partial negative charge results in a weaker attraction between the halogen and the CO_2 carbon atom, it also reduces the repulsion experienced by each electronegative oxygen atom on the sorbate. The net effect of all these interactions is a "balancing act" between the Br^- ions in MPM-1-Br, which is a unique feature compared to the Cl analog.

MPM-1-Cl is able to sorb more CO_2 overall than MPM-1-Br as demonstrated through both experimental measurements [37] and simulation (Figures 4 and 5). This could be due to the higher magnitude of the partial negative charge of the Cl^- ion as mentioned above. Electrostatic interactions are especially important for CO_2 sorption in both MPMs. It appears that the Coulombic attraction between the electropositive carbon atom of the CO_2 molecule and the halide ion increases with increasing partial negative charge of the anion. Further, the Cl^- ions tend to attract more electron density from the guest molecules via dispersive forces than the Br^- ions due to having a higher electronegativity.

The primary binding site for C_2H_2 in both MPM-1-Cl and MPM-1-Br is located near the copper paddlewheel complex, where the sorbate molecule orients parallel to the X–Cu–Cu–X axis (Figure 9). At this site, the center-of-mass (COM) of the C_2H_2 molecule is positioned approximately 5.5 and 5.2 Å away from the geometric center of the Cu^{2+} ions in MPM-1-Cl and MPM-1-Br, respectively. This particular alignment of the C_2H_2 molecule about the copper paddlewheels allows the positively charged H atom on both sides of the sorbate to interact with the electronegative halide ions that are coordinated to the Cu^{2+} ions. The negatively charged COM of the C_2H_2 molecule can also interact somewhat with the Cu^{2+} ions of the copper paddlewheels.

(a)   (b)

Figure 9. Molecular illustration of the primary binding site for C_2H_2 observed in (a) MPM-1-Cl and (b) MPM-1-Br through simulation, which is aligned with the X–Cu–Cu–X (X = Cl, Br) axis of the dinuclear copper paddlewheel complex. Atom colors are C = cyan; N = blue; H = white; Cu = brown; Cl = yellow; Br = red.

Overall, there are more concurrent interactions between the C_2H_2 molecule and the framework about the primary binding site in both MPMs relative to that for CO_2. Indeed, at the primary binding site, the C_2H_2 molecule exhibits two $H \cdots X^-$ and two $COM(C_2H_2) \cdots Cu^{2+}$ interactions. On the other hand, there are only two $C(CO_2) \cdots X^-$ interactions for CO_2 at the favorable binding site for this sorbate in both MPMs. The greater simultaneous interactions for C_2H_2 in MPM-1-X could explain why both MPMs display greater affinity and selectivity for C_2H_2 than CO_2. We note that the longer $COM(C_2H_2) \cdots Cu^{2+}$ distance for MPM-1-Cl results in slightly weaker affinity at this site relative to MPM-1-Br, thus potentially explaining why our simulations produced lower initial C_2H_2 Q_{st} values for the Cl analogue.

The results for the classical binding energy calculations from simulated annealing are presented in Table 2. It is clear from these simulations that both materials favor C_2H_2 over CO_2 (measured as a single molecule competition), which is consistent with experimental data. The energy minimum binding sites that were discovered through these simulations are the same as those shown in Figures 8 and 9. As observed in the results for the theoretical Q_{st} values (Table 1), the calculated binding energies for MPM-1-Br are higher than those for MPM-1-Cl. This is likely due to the higher polarizability of Br used in these simulations.

Table 2. Classical binding energies (in kJ mol^{-1}) for gases in MPM-1-Cl and MPM-1-Br as calculated by single-particle simulated annealing using the polarizable models for CO_2 and C_2H_2. The starting temperature for all simulations was 500 K, to ensure free and full exploration of the phase space of the system.

MPM-1-Cl	Binding energy (kJ mol^{-1})	Steps ($\times 10^6$)	Final Temp. (K)
CO_2	−26.3	2.37	113
C_2H_2	−29.9	2.46	125
MPM-1-Br			
CO_2	−28.2	3.24	129
C_2H_2	−34.7	4.53	150

5. Conclusions

This study aimed to elucidate the CO_2 and C_2H_2 sorption properties and mechanisms in two isostructural MPMs, MPM-1-Cl and MPM-1-Br. Our simulations revealed that MPM-1-Cl exhibits a better overall sorption capacity for both gases than MPM-1-Br, which is consistent with the experimental measurements reported by Xie et al. [37]. This could be due to a combination of larger accessible space in the Cl analogue at higher pressures (a consequence of the smaller ionic radius for Cl^-) and/or the fact that Cl is more electronegative than Br, which affords greater electrostatic interactions with the sorbate. At low loadings, however, the simulations suggest that MPM-1-Br is slightly more favorable toward both sorbates than MPM-1-Cl. We attribute this to the higher polarizablility and van der Waals parameters for the Br^- ions. Notably, repulsion/dispersion interactions could dominate the sorption mechanism at such loadings.

It was discovered through our simulations that the primary binding site for C_2H_2 and CO_2 in both MPMs are notably different between the two sorbates. Particularly, the C_2H_2 molecule prefers to align along the X–Cu–Cu–X axis of the copper paddlewheel to allow for favorable $H \cdots X^-$ interactions on each side of the molecule, while the CO_2 molecule seems to favor the region between the X^- ions of

two adjacent copper paddlewheel units. Both MPMs appear to be more selective toward C_2H_2 than CO_2 because there are a greater number of concurrent interactions about the primary binding site for C_2H_2.

Herein, we demonstrated how substitution of the halide ion in two isostructural MPMs with the empirical formula $[Cu_2(adenine)_4X_2]X_2$ affects the gas sorption properties in the material through molecular simulations. We plan to investigate the CO_2 and C_2H_2 sorption performance in MPM-1-TIFSIX [42] through theoretical studies in future work.

Acknowledgements

Conflict of interest

The authors declare no conflict of interest related to the content of this publication.

References

1. Zhou H, Long J, Yaghi O (2012) Introduction to Metal–Organic Frameworks. *Chem Rev* 112: 673–674.

2. Long J, Yaghi O (2009) The pervasive chemistry of metal–organic frameworks. *Chem Soc Rev* 38: 1213–1214.

3. Pham T, Forrest K, Franz D, et al. (2017) Experimental and theoretical investigations of the gas adsorption sites in rht-metal–organic frameworks. *CrystEngComm* 19: 4646–4665.

4. Nugent P, Belmabkhout Y, Burd S, et al. (2013) Porous materials with optimal adsorption thermodynamics and kinetics for CO_2 separation. *Nature* 495: 80–84.

5. Mason J, Sumida K, Herm Z, et al. (2011) Evaluating metal–organic frameworks for post-combustion carbon dioxide capture via temperature swing adsorption. *Energ Environ Sci* 4: 3030–3040.

6. Caskey S, Wong-Foy A, Matzger A (2008) Dramatic Tuning of Carbon Dioxide Uptake via Metal Substitution in a Coordination Polymer with Cylindrical Pores. *J Am Chem Soc* 130: 10870–10871.

7. Yang D, Cho H, Kim J, et al. (2012) CO_2 capture and conversion using Mg-MOF-74 prepared by a sonochemical method. *Energ Environ Sci* 5: 6465–6473.

8. Collins D, Zhou H (2007) Hydrogen storage in metal-organic frameworks. *J Mater Chem* 17: 3154–3160.

9. Collins D, Ma S, Zhou H (2010) Hydrogen and Methane Storage in Metal–Organic Frameworks, *Metal-Organic Frameworks: Design and Application*, John Wiley & Sons Inc., 249–266.

10. Suh M, Park H, Prasad T, et al. (2012) Hydrogen Storage in Metal–Organic Frameworks. *Chem Rev* 112: 782–835.

11. Lin X, Telepeni I, Blake A, et al. (2009) High Capacity Hydrogen Adsorption in Cu(II) Tetracarboxylate Framework Materials: The Role of Pore Size, Ligand Functionalization, and Exposed Metal Sites. *J Am Chem Soc* 131: 2159–2171.

12. Yan Y, Lin X, Yang S, et al. (2009) Exceptionally high H_2 storage by a metal–organic polyhedral framework. *Chem Commun* 1025–1027.

13. Mohammed M, Elsaidi S, Wojtas L, et al. (2012) Highly Selective CO_2 Uptake in Uninodal 6-Connected "mmo" Nets Based upon MO_4^{2-} (M = Cr, Mo) Pillars. *J Am Chem Soc* 134: 19556–19559.

14. Wu H, Yao K, Zhu Y, et al. (2012) Cu-TDPAT, an rht-Type Dual-Functional Metal–Organic Framework Offering Significant Potential for Use in H_2 and Natural Gas Purification Processes Operating at High Pressures. *J Phys Chem C* 116: 16609–16618.

15. Franz D, Forrest K, Pham T, et al. (2016) Accurate H_2 Sorption Modeling in the *rht*-MOF NOTT-112 Using Explicit Polarization. *Cryst Growth Des* 16: 6024–6032.

16. Pham T, Forrest K, Franz D, et al. (2017) Predictive models of gas sorption in a metal–organic framework with open-metal sites and small pore sizes. *Phys Chem Chem Phys* 19: 18587–18602.

17. Franz D, Dyott Z, Forrest K, et al. (2018) Simulations of hydrogen, carbon dioxide, and small hydrocarbon sorption in a nitrogen-rich rht-metal–organic framework. *Phys Chem Chem Phys* 20: 1761–1777.

18. Li J, Kuppler R, Zhou H (2009) Selective gas adsorption and separation in metal–organic frameworks. *Chem Soc Rev* 38: 1477–1504.

19. Wang H, Yao K, Zhang Z, et al. (2014) The first example of commensurate adsorption of atomic gas in a MOF and effective separation of xenon from other noble gases. *Chem Sci* 5: 620–624.

20. Lee J, Farha O, Roberts J, et al. (2009) Metal–organic framework materials as catalysts. *Chem Soc Rev* 5: 1450–1459.

21. Maeda C, Miyazaki Y, Ema T (2014) Recent progress in catalytic conversions of carbon dioxide. *Catal Sci Technol* 4: 1482–1497.

22. Cho S, Ma B, Nguyen S, et al. (2006) A metal–organic framework material that functions as an enantioselective catalyst for olefin epoxidation. *Chem Commun* 2563–2565.

23. Song J, Zhang Z, Hu S, et al. (2009) MOF-5/*n*-Bu$_4$NBr: an efficient catalyst system for the synthesis of cyclic carbonates from epoxides and CO_2 under mild conditions. *Green Chem* 11: 1031–1036.

24. Ma D, Li B, Zhou X, et al. (2013) A dual functional MOF as a luminescent sensor for quantitatively detecting the concentration of nitrobenzene and temperature. *Chem Commun* 8964–8966.

25. Wang J, Li M, Li D (2013) A dynamic, luminescent and entangled MOF as a qualitative sensor for volatile organic solvents and a quantitative monitor for acetonitrile vapour. *Chem Sci* 4: 1793–1801.

26. Larsen R, Wojtas L (2013) Photoinduced inter-cavity electron transfer between Ru(II)tris(2,2'-bipyridne) and Co(II)tris(2,2'-bipyridine) Co-encapsulated within a Zn(II)-trimesic acid metal organic framework. *J Mater Chem A* 1: 14133-14139.

27. Larsen R, Wojtas L (2012) Photophysical Studies of Ru(II)tris(2,2'-bipyridine) Confined within a Zn(II)–Trimesic Acid Polyhedral Metal–Organic Framework. *J Phys Chem A* 116: 7830–7835.

28. Whittington C, Wojtas L, Gao W, et al. (2015) A new photoactive Ru(II)tris(2,2'-bipyridine) templated Zn(II) benzene-1,4-dicarboxylate metal organic framework: structure and photophysical properties. *Dalton T* 44: 5331–5337.

29. Larsen R, Wojtas L (2015) Fixed distance photoinduced electron transfer between Fe and Zn porphyrins encapsulated within the Zn HKUST-1 metal organic framework. *Dalton T* 44: 2959–2963.

30. McKinlay A, Morris R, Horcajada P, et al. (2010) BioMOFs: metal–organic frameworks for biological and medical applications. *Angew Chem Int Edit* 49: 6260–6266.

31. Hinks N, McKinlay A, Xiao B, et al. (2010) Metal organic frameworks as NO delivery materials for biological applications. *Micropor Mesopor Mat* 129: 330–334.

32. Eddaoudi M, Moler D, Li H, et al. (2001) Modular Chemistry: Secondary Building Units as a Basis for the Design of Highly Porous and Robust Metal–Organic Carboxylate Frameworks. *Accounts Chem Res* 34: 319–330.

33. Nouar F, Eubank J, Bousquet T, et al. (2008) Supermolecular Building Blocks (SBBs) for the Design and Synthesis of Highly Porous Metal–Organic Frameworks. *J Am Chem Soc* 130: 1833–1835.

34. Figueroa J, Fout T, Plasynski S, et al. (2008) Advances in CO_2 capture technology—The U.S. Department of Energy's Carbon Sequestration Program. *Int J Greenh Gas Con* 2: 9–20.

35. Chen K, Scott H, Madden D, et al. (2016) Benchmark C_2H_2/CO_2 and CO_2/C_2H_2 Separation by Two Closely Related Hybrid Ultramicroporous Materials. *Chem* 1: 753–765.

36. Scott H, Shivanna M, Bajpai A, et al. (2017) Highly Selective Separation of C_2H_2 from CO_2 by a New Dichromate-Based Hybrid Ultramicroporous Material. *ACS Appl Mater Inter* 9: 33395–33400.

37. Xie DY, Xing HB, Zhang ZG, et al. (2017) Porous hydrogen-bonded organometallic frameworks for adsorption separation of acetylene and carbon dioxide. *CIESC J* 68: 154–162.

38. Thomas-Gipson J, Beobide G, Castillo O, et al. (2011) Porous supramolecular compound based on paddle-wheel shaped copper (II)–adenine dinuclear entities. *CrystEngComm* 13: 3301–3305.

39. Thomas-Gipson J, Beobide G, Castillo O, et al. (2014) Paddle-Wheel Shaped Copper(II)-Adenine Discrete Entities As Supramolecular Building Blocks To Afford Porous Supramolecular Metal–Organic Frameworks (SMOFs). *Cryst Growth Des* 14: 4019–4029.

40. Chui S, Lo S, Charmant J, et al. (1999) A Chemically Functionalizable Nanoporous Material $[Cu_3(TMA)_2(H_2O)_3]_n$. *Science* 283: 1148–1150.

41. Pham T, Forrest K, Chen K, et al. (2016) Theoretical Investigations of CO_2 and H_2 Sorption in Robust Molecular Porous Materials. *Langmuir* 32: 11492–11505.

42. Nugent P, Rhodus V, Pham T, et al. (2013) A robust molecular porous material with high CO_2 uptake and selectivity. *J Am Chem Soc* 68: 154–162.

43. Belof J, Stern A, Space B (2008) An Accurate and Transferable Intermolecular Diatomic Hydrogen Potential for Condensed Phase Simulation. *J Chem Theory Comput* 4: 1332–1337.

44. Rappé A, Casewit C, Colwell K, et al. (1992) UFF, a full periodic table force field for molecular mechanics and molecular dynamics simulations. *J Am Chem Soc* 114: 10024–10035.

45. Van Duijnen P, Swart M (1998) Molecular and Atomic Polarizabilities: Thole's Model Revisited. *J Phys Chem A* 102: 2399–2407.

46. Forrest K, Pham T, McLaughlin K, et al. (2012) Simulation of the Mechanism of Gas Sorption in a Metal–Organic Framework with Open Metal Sites: Molecular Hydrogen in PCN-61. *J Phys Chem C* 116: 155538–155549.

47. Breneman C, Wiberg K (1990) Determining atom-centered monopoles from molecular electrostatic potentials. The need for high sampling density in formamide conformational analysis. *J Comput Chem* 11: 361–373.

48. Valiev M, Bylaska EJ, Govind N, et al. (2010) NWChem: A comprehensive and scalable open-source solution for large scale molecular simulations. *Comput Phys Commun* 181: 1477–1489.

49. Mullen A, Pham T, Forrest K, et al. (2013) A Polarizable and Transferable PHAST CO_2 Potential for Materials Simulation. *J Chem Theory Comput* 9: 5421–5429.

50. Potoff J, Siepmann J (2001) Vapor–liquid equilibria of mixtures containing alkanes, carbon dioxide, and nitrogen. *AIChE J* 47: 16761682.

51. Metropolis N, Rosenbluth A, Rosenbluth M, et al. (1953) Equation of state calculations by fast computing machines. *J Chem Phys* 21: 1087–1092.

52. Massively Parallel Monte Carlo (MPMC), 2012. Available from: https://github.com/mpmccode/mpmc.

53. Monte Carlo-Molecular Dynamics (MCMD), 2017. Available from: https://github.com/khavernathy/mcmd.

54. Kirkpatrick S, Gelatt C, Vecchi M (1983) Optimization by Simulated Annealing. *Science* 220: 671–680.

55. Dincă M, Dailly A, Liu Y, et al. (2006) Hydrogen Storage in a Microporous Metal–Organic Framework with Exposed Mn^{2+} Coordination Sites. *J Am Chem Soc* 128: 16876–16883.

56. Pham T, Forrest K, McLaughlin K, et al. (2013) Theoretical Investigations of CO_2 and H_2 Sorption in an Interpenetrated Square-Pillared Metal–Organic Material. *J Phys Chem C* 117: 9970–9982.

57. Nicholson D, Parsonage N (1982) *Computer Simulation and the Statistical Mechanics of Adsorption*, Academic Press.

58. Bae Y, Mulfort K, Frost H, et al. (2008) Separation of CO_2 from CH_2 Using Mixed-Ligand Metal–Organic Frameworks. *Langmuir* 24: 8592–8598.

59. Goj A, Sholl D, Akten E, et al. (2002) Atomistic Simulations of CO_2 and N_2 Adsorption in Silica Zeolites: The Impact of Pore Size and Shape. *J Phys Chem B* 106: 8367–8375.

60.   Akten E, Siriwardane R, Sholl D (2003) Monte Carlo Simulation of Single- and Binary-Component Adsorption of CO_2, N_2, and H_2 in Zeolite Na-4A. *Energ Fuel* 17: 977–983.

61. Harris J, Yung K (1995) Carbon dioxide's liquid-vapor coexistence curve and critical properties as predicted by a simple molecular model. *J Phys Chem* 99: 12021–12024.